



Article

Influence of *Baccharis salicifolia* Extract on Iron Oxide Nanoparticles in MCM-41@IONP and Its Application in Room-Temperature-Fabricated Metal–Insulator–Semiconductor Diodes

Gerardo Miguel Bravo de Luciano ¹, Blanca Susana Soto-Cruz ¹, Anabel Romero-López ² ,
Yesmin Panecatí-Bernal ³ , José Alberto Luna-López ¹ and Miguel Ángel Domínguez-Jiménez ^{1,*}

¹ Centro de Investigación en Dispositivos Semiconductores, Instituto de Ciencias, Benemérita Universidad Autónoma de Puebla, Puebla 72570, Puebla, Mexico; gerardo.bravo@alumno.buap.mx (G.M.B.d.L.); blanca.soto@correo.buap.mx (B.S.S.-C.); jose.luna@correo.buap.mx (J.A.L.-L.)

² Instituto de Física “Luis Rivera Terrazas”, Benemérita Universidad Autónoma de Puebla, Ecocampus Valsequillo, San Pedro Zacachimalpa 72960, Puebla, Mexico; anabel.romero@correo.buap.mx

³ Ingeniería Industrial, Universidad Politécnica de Puebla, Tercer Carril del Ejido, Serrano s/n, Cuanalá 72640, Puebla, Mexico; yesmin.panecatí369@uppuebla.edu.mx

* Correspondence: miguel.dominguezj@correo.buap.mx; Tel.: +52-(222)-229-55-00 (ext. 1043)

Abstract: This work presents the green synthesis of iron oxide nanoparticles (IONPs) using *Baccharis salicifolia* extract and their incorporation in mesoporous silica MCM-41, obtaining an MCM-41@IONP composite. The MCM-41@IONP composite was characterized by X-ray diffraction (XRD), Fourier-transform infrared spectroscopy (FTIR), nitrogen adsorption and desorption, scanning electron microscopy (SEM) and energy-dispersive spectroscopy (EDS). The use of the natural reducing agent *Baccharis salicifolia* resulted in nanoparticles with an average size of 31 nm. Furthermore, we showcase the application of the MCM-41@IONP nanocomposite in a metal–insulator–semiconductor (MIS) diode, which was fabricated at room temperature. The current–voltage and capacitance–voltage curves of the MIS diode were carefully measured and subjected to detailed analysis. The results demonstrate the potential utility of MCM-41@IONP nanocomposite-based MIS diodes, suggesting their applicability in the design of biosensors or as discrete components in electronic devices.

Keywords: green synthesis; *Baccharis salicifolia*; composite; diode; nanoparticle; iron oxide



Citation: Bravo de Luciano, G.M.; Soto-Cruz, B.S.; Romero-López, A.; Panecatí-Bernal, Y.; Luna-López, J.A.; Domínguez-Jiménez, M.Á. Influence of *Baccharis salicifolia* Extract on Iron Oxide Nanoparticles in MCM-41@IONP and Its Application in Room-Temperature-Fabricated Metal–Insulator–Semiconductor Diodes. *Appl. Nano* **2024**, *5*, 58–71. <https://doi.org/10.3390/applnano5020006>

Academic Editor: Seokheun Choi

Received: 15 March 2024

Revised: 11 April 2024

Accepted: 17 April 2024

Published: 26 April 2024



Copyright: © 2024 by the authors. Licensee MDPI, Basel, Switzerland. This article is an open access article distributed under the terms and conditions of the Creative Commons Attribution (CC BY) license (<https://creativecommons.org/licenses/by/4.0/>).

1. Introduction

Electronic devices in industry are a cornerstone for the development of our daily lives [1] and scientific and technological advances [2]. Unfortunately, they are also the source of some of the largest amounts of pollution and waste generated by industries, with 53.6 million metric tons (Mt) of electronic waste being produced worldwide in 2019 alone, with a projected increase of more than 74.7 Mt by 2030 due to the high demand [3,4]. This poses a significant environmental problem because of the substantial consumption of non-renewable raw materials, commonly including rare earths and toxic metallic and non-metallic elements. Additionally, there is a considerable amount of energy required for their mass production [5].

For a couple of decades, and to counteract the aforementioned problems, great attention has been paid to the synthesis and manufacture of new materials, less toxic products, renewable sources of energy and raw materials, and energy-efficient industrial processes [6]. For this purpose, the 12 principles indicated since 1998 by Paul Anastas and John Warner have been taken up again [7], promoting a philosophy which establishes high standards in research and chemical processes that eliminate the use of substances that are hazardous to living beings and the environment and seeking a sustainable future with an increase in life quality [8].

Even though there have been materials considered organic semiconductors since 1950 and they have captured the attention of the scientific community due to their ideal characteristics for new technologies (nanometric size, low or zero toxicity, abundant material, easy to produce, cheap, and with feasible production conditions), until the last decade, only a few had been directly used for the development of electronic devices [9].

Among them, we have nanoparticles incorporated in porous matrices, such as iron oxide nanoparticles (IONPs), which possess unique properties, including a large surface-to-volume ratio [10], magnetism (magnetite and maghemite), high surface energies, and high chemical activity [11]. The last property makes them highly reactive if left uncovered, oxidizing easily upon contact with the air, leading to the loss of or decrease in some of their properties. To prevent this, it is essential to provide a protective coating to maintain their stability and properties over a longer period. In conclusion, the incorporation of IONPs with another material can preserve their unique properties [12].

MCM-41 seems to be a promising alternative as a porous material, featuring a hexagonal pore arrangement with a uniform pore size in the range of 10 to 1000 Å; a large surface area (700 to 1500 m² g⁻¹); and high thermal, chemical, and mechanical stability [13,14]. Therefore, it holds great potential for incorporating various types of materials, including nanoparticles [15].

For the preparation of this MCM-41@IONP nanocomposite, various synthesis methods are available, including both in situ and ex situ. These methods involve the use of synthetic reductants or stabilizing agents, such as oleic acid (OA), oleylamine (OAm), and 1-octadecene (ODE) [16]; polyethylene glycol and hydrochloric acid [17]; hydrochloric acid solution and ammonium solution [18]; triblock copolymer (Pluronic 123, EO20, PO70, EO20) [19]; and hydrothermal processes [20], among others. Unfortunately, these methods contribute to environmental pollution. To address this issue, there has been a proposal to replace anthropogenic chemical agents used in conventional methods with extracts from plants (phytochemicals) as natural and eco-friendly chemical agents [21].

In recent years, the synthesis of green iron oxide nanoparticles (IONPs) incorporated in mesoporous silica using *Camellia sinensis* (black tea) leaf extract as a bioreducing and stabilizing agent [22] has been reported. Additionally, the synthesis of IONPs using natural extracts from various plants including *Mentha pulegium* L. [23], *Lagenaria siceraria* [24], *Avicennia marina* flower [25], *Platanus orientalis* [26], *Phyllanthus niruri* [27], *Daphne mezereum* [28], seeds, *Psoralea corylifolia* [29], and *Punica granatum* [30] and roots such as *Mimosa pudica* [31] has been reported in the literature.

The plant was selected because it is very abundant and is easily produced; it can be grown in extreme atmospheric conditions, and even in environments with high concentrations of pollutants, without having any effect on its growth and development [32]. A study conducted in 2008 by Haque et al. revealed, using a specimen of the same family (*Baccharis sarothroides* Gray), that it is a potential hyperaccumulator of pollutants such as lead (Pb), chromium (Cr), and arsenic (As), among others, being considered a phytoremediator element of soils. Therefore, this work proposes this type of plant as an object of interest due to its properties, which continue to be studied in depth to determine its potential application in other areas [33].

This work presents a route for the synthesis and incorporation of environmentally friendly IONP in MCM-41 from an alternative natural extract (*Baccharis salicifolia*) and presents its properties, which have not been studied yet. It offers advantages over other extracts which have been used, such as its abundance and capacity for adaptation to extreme conditions (despite being endemic to Central and South America) which ensure high availability at any time of the year. Moreover, its application in a metal-insulator-semiconductor (MIS) diode fabricated at room temperature is demonstrated. It can be used as a feasible detector of various dangerous gases and contaminants because its construction is low cost, they have a fast response and high sensitivity, and, thanks to the coating that MCM-41 provides to IONPs, reported deficiencies [34] decrease or may even disappear. In addition, as mentioned by Hasanzadeh et al. in 2013, using the MCM-41-Fe₂O₃ material as

a biosensor creates new capabilities in the field of electrochemical detection by combining the properties of Fe₂O₃ magnetic nanoparticles and the large surface area of MCM-41 [35].

2. Materials and Methods

Analytical-grade iron (II) sulfate was used as the precursor and MCM-41 (Sigma Aldrich, St. Louis, MO, USA) served as the mesoporous matrix. For the extract, leaves of *Baccharis salicifolia* were collected in the city of Puebla (Mexico) in June 2022. After air drying, the leaves were crushed into small pieces by hand, and then, a porcelain mortar was used to pulverize the leaves. To identify the best solvent, the spray was mixed with water and ethanol and each extraction was carried out at a different temperature (see Table 1). The general process involved soaking 4 g of leaves in 100 mL of solvent and leaving them for 3 min at a specific temperature. Finally, all plant residues were removed by filtration. The synthesis of iron oxide nanoparticles was carried out through green chemistry. The extract was prepared from *Baccharis salicifolia* leaves and 0.01–0.005 M FeSO₄ solutions, mixed in a ratio of 2:5 and homogenized by means of a magnetic stirrer at different conditions of atmosphere and temperature (see Table 1). After 1 h, the darkening of the solutions was observed in all samples. Some factors such as the volume and concentration of the precursors were optimized in the synthesis of IONPs.

Table 1. IONP synthesis conditions.

Sample	Agent Reductor	Temperature	Solvent	Atmosphere	Precursor Concentration (M)	Particle Size (nm)
1	<i>Baccharis salicifolia</i>	100 °C	Water	Air	0.005	779
2	<i>Baccharis salicifolia</i>	25 °C	Water	Air	0.005	597.1
3	<i>Baccharis salicifolia</i>	100 °C	Water	Nitrogen	0.005	479.4
4	<i>Baccharis salicifolia</i>	25 °C	Water	Nitrogen	0.005	408
5	<i>Baccharis salicifolia</i>	100 °C	Water	Nitrogen	0.01	306.3
6	<i>Baccharis salicifolia</i>	80 °C	Water	Nitrogen	0.01	228.4
7	<i>Baccharis salicifolia</i>	80 °C	Ethanol	Nitrogen	0.005	146.7
8	<i>Baccharis salicifolia</i>	80 °C	Ethanol	Nitrogen	0.01	31.17
9	<i>Baccharis salicifolia</i>	25 °C	Ethanol	Nitrogen	0.01	83

To identify the size of the nanoparticles, the dynamic light scattering (DLS) technique was used, placing the dispersion (3 mL of the solution) in an ultrasonic tip for 20 min. The synthesis of the MCM-41@IONP nanocomposite was carried out ex situ by weighing 20 mg of MCM-41, drying it at 150 °C for 12 h in a muffle (1200 °C Thermo Scientific—Thermolyne; Waltham, MA, USA), keeping it in a nitrogen atmosphere, and magnetically stirring it at 78 °C on a grill (MS7-H550-PRO, BIOBASE, Jinan, China). Subsequently, the extract prepared from *Baccharis salicifolia* leaves and the 0.01–0.005 M FeSO₄ solution were added in a ratio of 2:5 mL. After 1 h of maintaining the conditions, the sample was filtered and dried at 35 °C.

The techniques used to characterize the compound were X-ray diffraction (XRD), scanning electron microscopy (SEM), energy-dispersive spectroscopy (EDS), nitrogen adsorption and desorption, and Fourier-transform infrared spectroscopy (FTIR), which are techniques that provide detailed information about the following aspects: Crystalline structure, which helps us to identify the crystalline phases of the porous material and size of the crystals [36]. The porosity of a material, which helps to analyze the surface, pore-size distribution, and adsorption capacity [37]. Composition, which identifies the functional groups present in a porous material and in the incorporated nanoparticles. These aspects are essential to allow reproducibility and to optimize properties and applications [38].

For the incorporation process, 20 mg of MCM-41 was weighed in an Erlenmeyer flask and placed for 12 h in a muffle at 150 °C to extract moisture. After that, a neoprene cap was placed on it to prevent it from absorbing humidity from the environment, and it was allowed to cool at room temperature. Subsequently, a nitrogen atmosphere was injected and placed under stirring at a temperature of 80 °C to add the reducing agent (*Baharis sacifolia* extract). Once it was completely added, it was left to be stirred for a few seconds to homogenize the sample, and the addition of the iron precursor was continued by dripping 1 drop/second of FeSO₄ [0.01] M in a ratio of 5:2. Once the addition of the precursor was completed, it was left under magnetic stirring for one hour, maintaining the conditions.

The films were deposited from a homogeneous solution of the MCM-41@IONP sample on an N-type silicon substrate with an orientation of (100) with a resistivity of 1–5 Ωcm. For the deposition process, 3 mg of synthesized MCM-41@IONP powder was weighed and 5 mL of ethanol was added. This mixture was magnetically stirred for 24 h and then subjected to ultrasonic treatment for 2 more hours. The deposition of 4 layers was carried out successively by spin-coating (Laurell WS-650 spin coater, Laurell Technologies, Lansdale, PA, USA) at 3000 RPM for 45 s each one. The thickness of the MCM-41@IONP thin film was approximately 61 nm. No additional heat treatments were performed. The gold contacts were deposited by the sputtering technique, as illustrated in Figure 1a, to obtain the MIS devices illustrated in Figure 1b. The fabrication of the MIS diodes was performed at room temperature. The top electrode area was 1 mm².

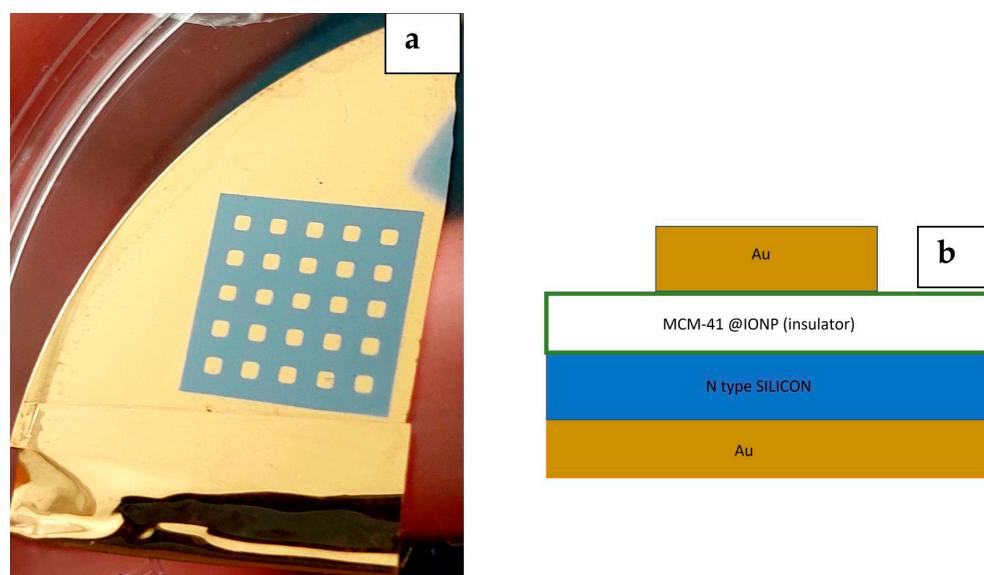


Figure 1. Room-temperature-fabricated MIS devices. (a) Photograph, (b) cross-section.

3. Results

The information on the chemical composition of *Baccharis salicifolia* extract is not accurate, as different sources do not completely agree. However, there is a consensus that it primarily contains terpenoids and their derivations [39,40]. According to several authors, some of the phytochemicals found in higher concentrations include β -cariophyllene, germacrene, β -ocimene, 6,9-guaiadiene, germacrene-D, α -phellandrene, and α -cubebene [11,41], as illustrated in Figure 2. These types of natural chemicals are used as particle-reducing agents, so the plant-selection process is considered important.

The relation between the particle size of iron oxide and the different reaction conditions, including the temperature, concentration of iron precursor, reducing agent, etc., has been extensively studied in the literature [42,43]. Table 1 summarizes the preparation conditions of the different samples. The synthesis parameters, such as concentration and temperature, were varied and controlled in each case. The influence of these parameters on the particle-size distribution was determined by dynamic light scattering (DLS) measurements, with

the stirring time being kept constant for all samples (one hour of magnetic stirring). We present the different reaction conditions used in the synthesis of IONPs, observing that, in addition to the influence of the ferrous sulfate concentration, which is not invariably proportional to the increase in the precursor concentration, a higher concentration of the precursor leads to increased nucleation. It has been reported that during the growth phase, there are two different moments, an initial one where the size reaches a maximum as the precursor increases and the second one where an increase in precursor concentration results in a decrease in growth [44,45]. Other parameters influencing the nucleation stage and particle growth include temperature. Temperature plays a very important role; a higher temperature leads to the increased kinetic energy of the particles, raising the reaction rate and resulting in larger particle sizes.

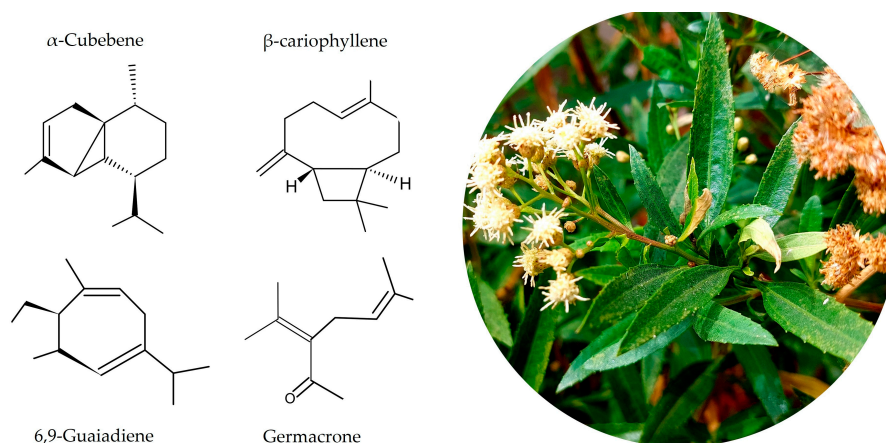


Figure 2. Structures of the phytochemicals with the highest concentration in the extract of *Baccharis salicifolia*.

Figure 3 shows the smallest particle size obtained from iron oxide nanoparticles synthesized using *Baccharis salicifolia* leaf extract as the reducing agent, with an average hydro-dynamic diameter of 31.17 nm with a dispersion of 91.7%, corresponding to synthesis route 8, as indicated in Table 1. This synthesis was considered the most reliable, because it produced the smallest particle size among all the syntheses tested, as shown in Figure S1a–i. This is a very important factor, because MCM-41 has an approximate pore diameter of 3–6 nanometers, as shown in Figure S2. Therefore, for the incorporation of the nanoparticles into the pores, it was necessary to use an extract that would allow the formation of dwarf particles of the smallest possible size.

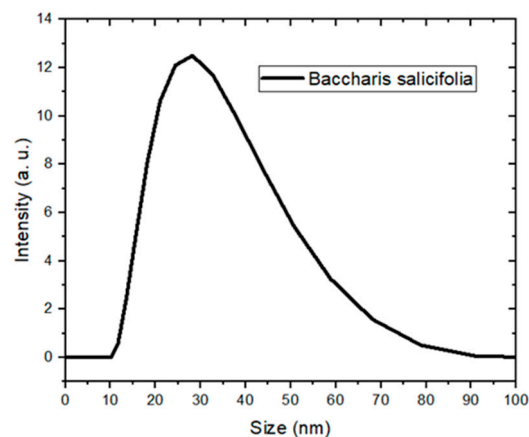


Figure 3. Average-size iron oxide particles.

Figure 4 shows the XRD pattern of the MCM-41 (black) and MCM-41@IONP composite (red) at low angles. Since the supporting matrix for the nanoparticles is MCM-41, characterized by PDF 00-049-1712 from International Centre for Diffraction Data (ICDD) [46], three characteristic peaks are observed. The first peak at $2\theta = 2.01^\circ$ (100) is the most intense, while the remaining two peaks at $2\theta = 3.67^\circ$ (110) and at $2\theta = 4.2^\circ$ (200) have lower intensities. Interestingly, the XRD pattern of MCM-41 @IONP shows only one plane at $2\theta = 2.26^\circ$ (100), which is less intense, with the (110) and (200) planes being absent in the pattern. The interplanar spacing distances for the (100) peak were determined at 21.9 nm for MCM-41 and 19.5 nm for the MCM-41@IONP sample, as well as their lattice parameters at 25.35 nm and 22.55 nm, respectively [47].

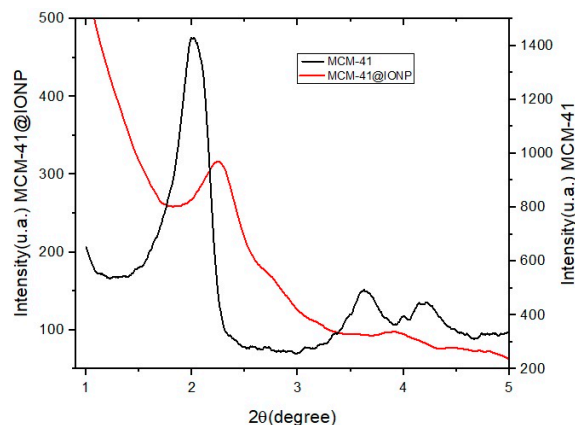


Figure 4. Low-angle X-ray diffraction spectra of MCM-41 (black) and MCM-41@IONP (red) sample.

Figure 5 shows the nitrogen adsorption–desorption isotherms of both the pure MCM-41 sample (black) and that of MCM-41@IONP (red). The general pattern that we observed in both samples is type IV according to the IUPAC classification. This type of isotherm is a characteristic of materials with a pore size in the range of 2 to 50 nm, belonging to mesopores with well-defined and uniform size distribution.

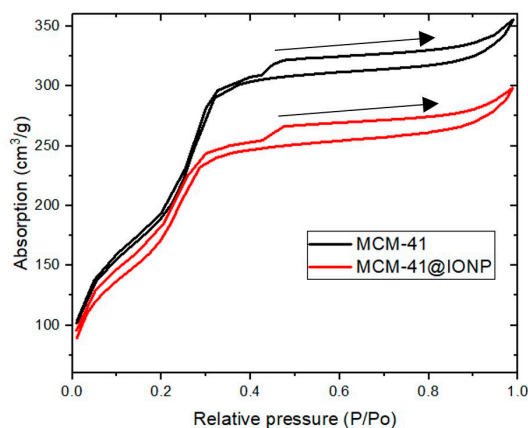


Figure 5. Comparison of nitrogen adsorption (arrow) and desorption isotherms for pure MCM-41 (black) and MCM-41@IONP (red).

We can clearly see that both isotherms present four well-defined regions: Region I: This corresponds to the region of low adsorption pressures (0.0–0.32) for MCM-41 and (0.01–0.35) for MCM-41@IONP; in this part, the isotherm shows a very large slope. This is due to the increase in the adsorption amount by the rapid occupation of the adsorption sites in the pores. Region II: The adsorption begins to be slower, so the slope decreases considerably because the adsorption sites within the pores have been filling; it does not mean that the adsorption has reached its limit, since there are still available pores for

adsorption. However, an adsorption process begins to occur on the external surface of the material [48]. Region III: This corresponds to high adsorption pressures > 0.4 ; adsorption continues but is slower, where a monolayer begins to form both on the outside and in the pores of the material. Region IV: Even though adsorption continues, the mesopores and the external surface of the material are saturated, so additional layers of adsorbed molecules begin to form on the existing monolayer of the material [49].

On the other hand, the discrepancy between the adsorption and desorption paths (called hysteresis) is noticeable. It is formed due to the different interactions of the molecules with the surface of the material during physisorption. Having a very large porous structure with a defined pore-size distribution can give a rise to different adsorption and desorption mechanisms of the molecules [50]. In both samples, we can observe that the hysteresis formed is of the H2 type, which is common in mesoporous materials and suggests the presence of uniform cylindrical pores that form a well-defined three-dimensional porous structure [51].

Figure 6 presents SEM images comparing MCM-41 (a, c) and MCM-41@IONP (b, d) at different magnification scales, 1 μm and 500 nm, revealing significant differences. One of them is the contrasting MCM-41 (Figure 6a), which shows a marked contrast, making visibility challenging due to the dielectric nature of the material. In contrast, the MCM-41@IONP sample (Figure 6b) shows less contrast, facilitating material visualization because of the presence of iron which enhances conductivity and brightens the image of the material with iron nanoparticles. Additionally, Figure 6c provides the porous areas of the material, while Figure 6d demonstrates a reduction in porosity after the incorporation of the iron oxide nanoparticles. Although this reduction may seemingly decrease the absorption capacity of the original material (by occupying pores), it introduces other properties inherent to IONPs, such as a large and reactive surface chemistry [52], which can interact and influence the mobility of different substances based on their application, in addition to providing potential catalytic and magnetic properties [12].

The energy-dispersive X-ray spectrum (EDS) confirms the presence of Si, Fe, C, and O species in the structure of the material. Table 2 shows the comparative values obtained by EDS analysis, representing the elemental composition in mass percentage for both the MCM-41 and MCM-41@IONP samples.

Table 2. Comparison of the elemental content and mass percentage of the MCM-41 and MCM-41@IONP samples.

	SiO ₂ %	Fe ₂ O ₃ /Fe ₃ O ₄ %	Na ₂ O %	Al ₂ O ₃ %	C %	Total %
MCM-41	85.86	-----	4.36	1.6	8.18	100
MCM-41@IONP	68.44	2.14	0.24	1.28	30.04	100

The elemental mapping of the MCM-41@IONP nanocomposite (Figure 7) was obtained. It shows the elements presented in Table 2, showing their spatial location.

Figure 8 shows the FTIR spectra of MCM-41 and MCM-41@IONP. The pure MCM-41 material (in black) exhibits bands at 445 cm^{-1} and 800 cm^{-1} , corresponding to the Si-O bonds; at 1097 cm^{-1} and 16290 cm^{-1} , related to the Si-O-Si bonds; and at 3435 cm^{-1} , indicative of OH bonds, according to the literature [53]. Conversely, the spectrum of the MCM-41@IONP material (in red) shows the presence of absorption bands of two different iron oxides at 1080 cm^{-1} , 1633 cm^{-1} , and 2916 cm^{-1} , which are typical vibrations of Fe₂O₃ [54–56].

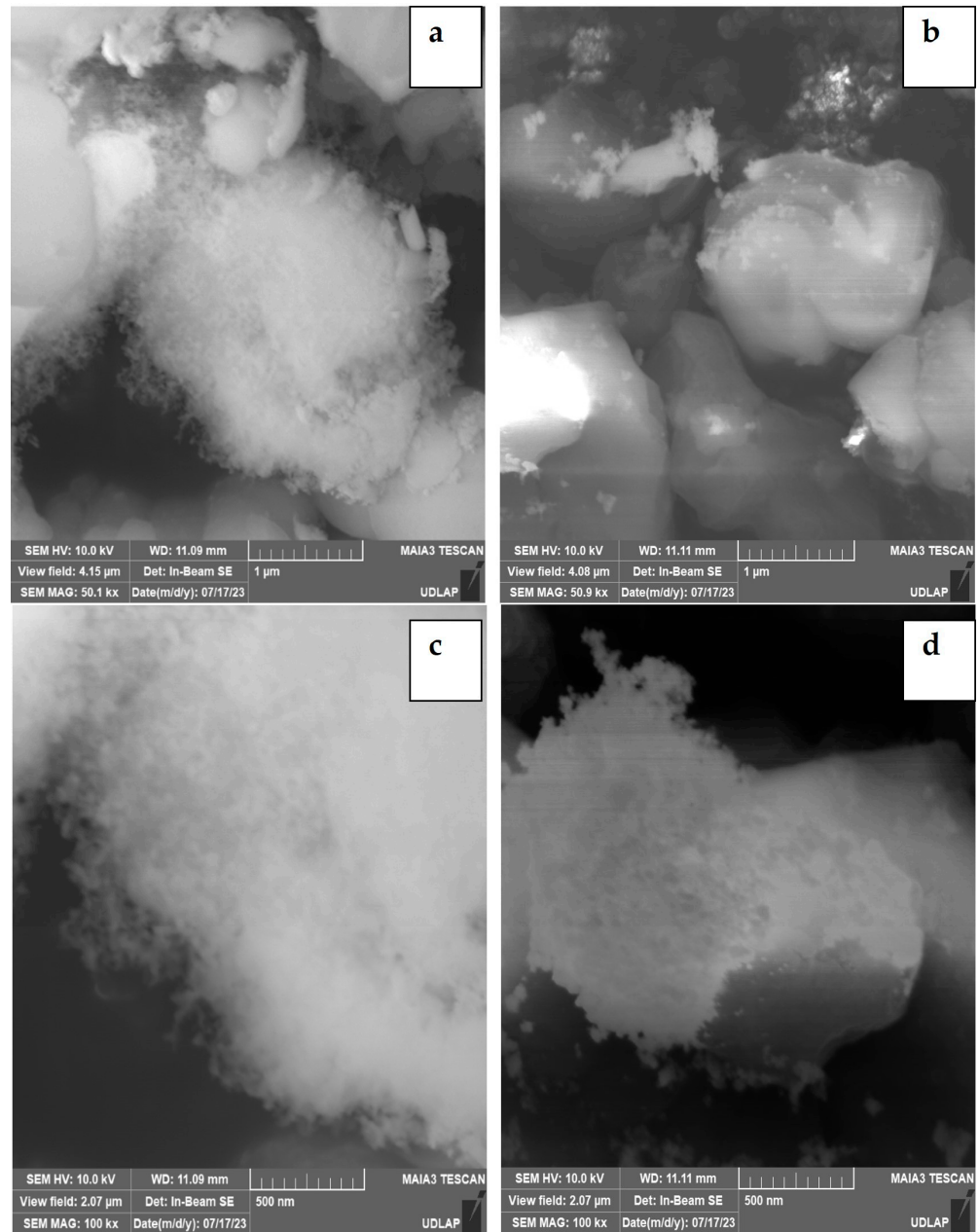


Figure 6. SEM Images with zoom scales at 1 μm and 500 nm: (a) 1 μm scale MCM-41, (b) 1 μm scale MCM-41@IONP, (c) 500 nm scale MCM-41, (d) 500 nm scale MCM-41@IONP.

In this work, MIS diodes were fabricated using spin-coating deposition, incorporating a layer of iron oxide nanoparticles into an MCM-41 matrix. Four layers were sequentially deposited to form a homogeneous film of approximately 61 nm thickness at room temperature on n-type silicon wafers. Each layer was spin-coated immediately after the other one, and the entire deposition process took about 10 min.

Figure 9 shows the current–voltage (I – V) curves of the MIS diodes. When a negative voltage is applied to the top contact, the current remains independent of the voltage applied, demonstrating good rectifying behavior. On the other hand, applying a positive voltage to the top contact results in carriers being injected through the MCM-41 material, leading to an exponential increase in current with applied bias.

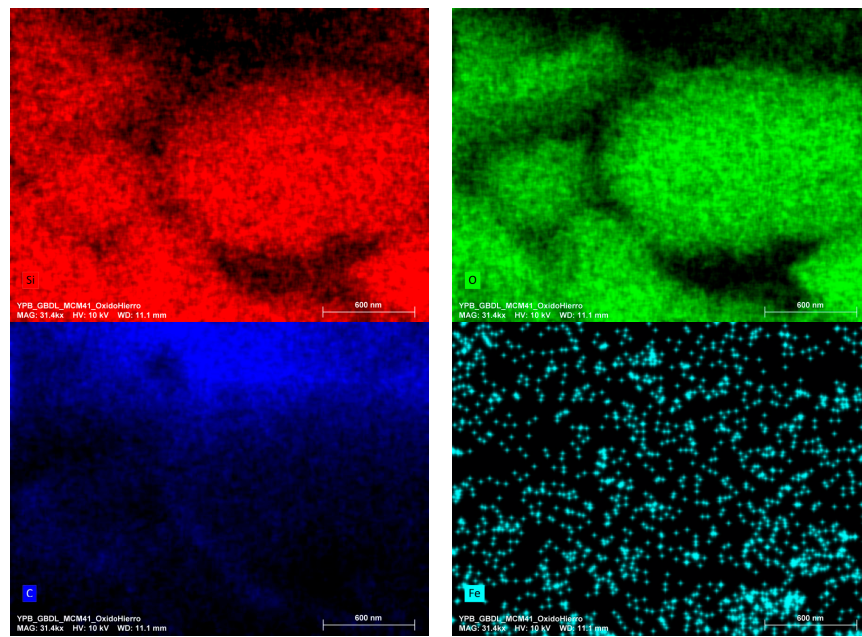


Figure 7. Elemental maps of Si (red), oxygen (green), carbon (blue) and iron (cyan) atoms in the MCM-41@IONP material.

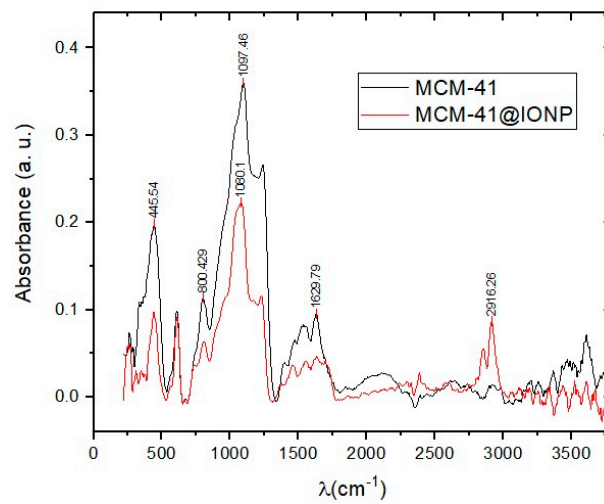


Figure 8. Comparative FTIR spectra of sample MCM-41 (black) and MCM-41@IONP (red).

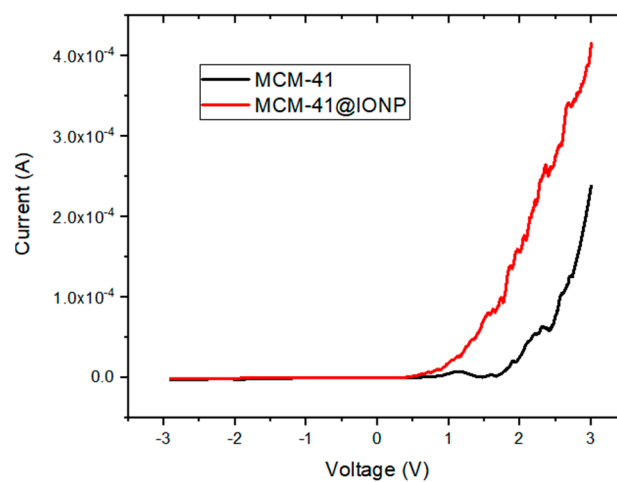


Figure 9. I–V comparison of an MIS diode MCM-41 (black) and MCM-41@IONP (red).

Figure 10 presents the capacitance–voltage (C–V) curves of the MIS diodes. In Figure 10, the C–V curve of MCM-41 (black), shows well-defined accumulation and depletion regions under positive and negative bias, respectively. In Figure 10, the C–V curve of the MCM-41@IONP composite (red) is presented. Interestingly, while the depletion region is clearly identified, the accumulation region is not fully reached.

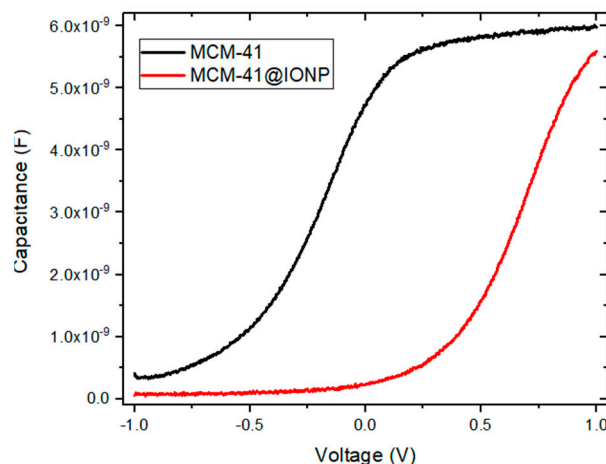


Figure 10. C–V comparison of an MIS diode MCM-41 (black) and MCM-41@IONP (red) at low frequency (1 kHz).

4. Discussion

This type of metal–insulator–semiconductor diode structure can be used as a sensor device for biomolecular interactions such as DNA hybridization, as reported by Migliorato et al. in 2004 [57].

From the XRD analysis, we were able to calculate the interplanar spacing using data from the peak (100), as shown in Table 3. It is observed that this peak decreases in intensity in comparison to pure MCM-41, as reported in the literature [44]. This decrease is attributed to the alteration in the crystalline network of the material, leading to the absence of the other two characteristic peaks. This is a consequence of the presence of the IONPs in MCM-41. These findings align with the results obtained from nitrogen adsorption characterization, which indicates that pure MCM-41 has a greater adsorption volume due to its high porosity, with most of its pores being available [58]. On the other hand, the MCM-41@IONP sample presents a lower adsorption volume. This reduction in surface area and pore volume is a result of the presence of iron oxide nanoparticles within them, gradually filling the pores and decreasing the adsorption capacity [59]. This not only confirms the effectiveness of our green synthesis and incorporation route but also suggests that the IONPs are attached to the pores and may be smaller than indicated by DLS [60], as shown in Figure S2. Although there is an alteration in the crystalline network of MCM-41 due to the presence of iron oxide nanoparticles, this is not significant since the sizes of the pores, as well as their isothermal profiles, are not significantly altered. This is possible because the synthesis and incorporation of the IONPs in MCM-41 was carried out by an in situ method, where the IONPs were incorporated into the pores of MCM-41. Therefore, the nucleation and growth of nanoparticles is limited, which can be translated to a smaller size and uniform distribution of IONPs [61].

The morphological analysis SEM images of the pure MCM-41 samples reveal areas with high densities of pores, with most of the clusters exhibiting diffuse contours (porous zones). Conversely, images of the MCM-41@IONP composite show a lower concentration of these porous areas, resulting in the appearance of well-defined geometric shapes in the sample. This change is attributed to the incorporation of iron oxide nanoparticles that fill part of the pores.

Table 3. The lattice parameters and textural properties of MCM-41 and MCM-41@IONP.

Sample	θ_{100} ^a	d_{100} ^b (nm)	a_0 ^c (nm)	S_{BET} ^d (m ² g ⁻¹)	Pore Radius ^e (nm)
MCM-41	2.01	21.9	25.35	2726	1.26
MCM-41@IONP	2.26	19.5	22.55	3128	1.15

^a Angle (100). ^b Interplanar distance. ^c Lattice parameter. ^d surface area. ^e Pore radius by BJH method.

Table 3 shows a comparative summary of the lattice parameters and structural properties of MCM-41 and MCM-41@IONP.

In the compositional analysis, the presence of oxygen and silicon (SiO₂) in the MCM-41 sample is confirmed, with silicon being predominant due to the nature of the material. In contrast, the MCM-41@IONP sample confirms the presence of the iron element, indicating the successful incorporation of iron oxide nanoparticles. Elemental maps of the synthesized composite depict well-dispersed IONP nanoparticles. The image of the selected area reveals the homogeneous presence of Fe throughout the sample, confirming the uniformity of the synthesized material.

The identification of the iron oxide species present in our material was carried out thanks to the comparison of the absorption peaks in the FT-IR spectra between the pure MCM-41 [53] and the MCM-41@IONP composite, which confirmed that the iron species observed in the EDS spectral image belong to nanoparticles of two different types of iron oxides, maghemite and magnetite [52–55].

MCM-41 is a mesoporous silicon dioxide thin film, which exhibits the dielectric properties characteristic of an insulator layer according to the C–V curve in Figure 10. However, as can be seen in Figure 9, the current in MCM-41 exhibits rectifying behavior. This can be explained due to the mesoporous structure of the thin film, which affects its dielectric behavior. When a negative voltage is applied to the top contact, the depletion region increases at the MCM-41/silicon and MCM-41@IONP/silicon interfaces, resulting in an independent current with voltage applied. Meanwhile, with a positive voltage, the carriers accumulate at the MCM-41/silicon and MCM-41@IONP/silicon interfaces, leading to an increase in current, presumably through carrier tunneling [62,63]. Interestingly, the current of the MCM-41@IONP diode is higher than that of the MCM-41 diode, which can be related to the incorporation of the iron oxide nanoparticles. In MCM-41@IONP, the nanoparticles affect the dielectric behavior of the MCM-41 thin film. This behavior aligns with the C–V curves, since the MCM-41@IONP sample shows a characteristic diode curve, where the accumulation region is not completely defined due to the increased current [62]. Further research is needed to confirm the transport mechanism of these MIS diodes and their potential application as biosensors.

5. Conclusions

In this study, we analyzed the effect of the synthesis and the efficiency of phytochemicals present in plant extracts on the size of IONPs. The optimal synthesis conditions were achieved by utilizing *Baccharis salicifolia* extract as a reducing and stabilizing agent for both IONPs and their incorporation into an MCM-41 matrix, forming the MCM-41@IONP nanocomposite. This process was carried out using a low-cost and rapid green chemistry method. Structural, textural, morphological, and optical analyses revealed the successful synthesis of IONPs, including two different species, maghemite and magnetite, with sizes in the range of around 31.71 nm. These nanoparticles were effectively incorporated into the mesoporous structure of MCM-41, preventing agglomeration. Furthermore, we demonstrated that the MCM-41@IONP nanocomposite thin film holds potential for the development of an MIS device. This device could be applied in the design of biosensors and sensors or as a discrete component of electronic devices.

Supplementary Materials: The following supporting information can be downloaded at <https://www.mdpi.com/article/10.3390/applnano5020006/s1>, Figure S1: (a–i) Particle size distribution by DLS of the samples; Figure S2: Comparison of pore size distributions of MCM-41 and MCM-41@IONP; Figure S3: The high angle X-ray diffraction pattern of the MCM-41@IONP; Figure S4: General scheme of the synthesis methodology, incorporation of iron oxide nanoparticles and construction of the MIS-type device.

Author Contributions: Conceptualization, G.M.B.d.L., B.S.S.-C. and Y.P.-B.; methodology, Y.P.-B., B.S.S.-C. and M.Á.D.-J.; validation, B.S.S.-C., A.R.-L., J.A.L.-L. and M.Á.D.-J.; formal analysis, G.M.B.d.L., B.S.S.-C., A.R.-L. and M.Á.D.-J.; research, G.M.B.d.L. and J.A.L.-L.; writing: preparation of the original draft, G.M.B.d.L.; writing: review and editing, B.S.S.-C., A.R.-L., Y.P.-B., J.A.L.-L. and M.Á.D.-J.; supervision, B.S.S.-C. and M.Á.D.-J.; project management, B.S.S.-C. and M.Á.D.-J.; financing acquisition, B.S.S.-C., J.A.L.-L. and M.Á.D.-J. All authors have read and agreed to the published version of the manuscript.

Funding: This work was partially supported by Fondo Sectorial de Investigación para la Educación CONACyT-SEP [A1-S-7888] and Proyectos VIEP-BUAP.

Data Availability Statement: This article has no associated data. Data related to this work are available in the manuscript.

Acknowledgments: The authors would like to acknowledge CONACYT for the doctoral scholarship (770598) and the Department of Chemistry and Biological Sciences at the University of the Americas Puebla (UDLAP) for the SEM characterization.

Conflicts of Interest: The authors declare that there are no conflicts of interest regarding the publication of this paper.

References

1. Rashid, S.M.; Mawah, J.; Banik, E.; Akter, Y.; Deen, J.I.; Jahan, A.; Khan, N.M.; Rahman, M.M.; Lipi, N.; Akter, F.; et al. Prevalence and impact of the use of electronic gadgets on the health of children in secondary schools in Bangladesh: A cross-sectional study. *Health Sci. Rep.* **2021**, *4*, e388. [[CrossRef](#)]
2. García, F.P.; Talapin, D.V.; Klimov, V.I.; Arakawa, Y.; Bayer, M.; Sargent, E.H. Semiconductor quantum dots: Technological progress and future challenges. *J. Sci.* **2021**, *373*, 6555. [[CrossRef](#)]
3. Forti, V.; Balde, C.P.; Kuehr, R.; Bel, G. *The Global E-Waste Monitor 2020: Quantities, Flows and the Circular Economy Potential*; United Nations University: Bonn, Germany; United Nations Institute for Training and Research; International Telecommunication Union: Geneva, Switzerland; International Solid Waste Association: Rotterdam, The Netherlands, 2020.
4. Ghimire, H.; Ariya, P.A. E-Wastes: Bridging the Knowledge Gaps in Global Production Budgets, Composition, Recycling and Sustainability Implications. *Sustain. Chem.* **2020**, *1*, 154–182. [[CrossRef](#)]
5. Huang, Y.; Cohen, T.A.; Parker, C.K.; Luscombe, C.K. Green syntheses of stable and efficient organic dyes for organic hybrid light-emitting diodes. *J. Mater. Chem.* **2021**, *9*, 7274–7283. [[CrossRef](#)]
6. Warner, J.C.; Cannon, S.A.; Dye, M.K. Green Chemistry. *Environ. Impact Assess. Rev.* **2004**, *24*, 775–799. [[CrossRef](#)]
7. Anastas, P.T.; Warner, J.C. *Green Chemistry: Theory and Practice*; Oxford University Press: New York, NY, USA, 1998; p. 30.
8. Kharissova, V.O.; Kharisov, I.B.; González, O.C.; Méndez, P.Y.; López, I. Greener synthesis of chemical compounds and materials. *R. Soc. Open Sci.* **2019**, *6*, 191378. [[CrossRef](#)]
9. Mabindisa, R.; Tambwe, K.; Mciteka, L.; Ross, N. Organic Nanostructured Materials for Sustainable Application in Next Generation Solar Cells. *Appl. Sci.* **2021**, *11*, 11324. [[CrossRef](#)]
10. Tai, C.V.; Che, H.X.; Kong, X.Y.; Ho, K.C.; Ng, W.M. Decoding iron oxide nanoparticles from design and development to real world application in water remediation. *J. Ind. Eng. Chem.* **2023**, *127*, 82–100. [[CrossRef](#)]
11. Vargas, O.J.; Gonzalez, C.; Esquivel, K. Magnetic Iron Nanoparticles: Synthesis, Surface Enhancements, and Biological Challenges. *Processes* **2022**, *10*, 2282. [[CrossRef](#)]
12. Ali, A.; Zafar, H.; Zia, M.; Haq, U.I.; Phull, A.R.; Ali, J.S.; Hussain, A. Synthesis, characterization, applications, and challenges of iron oxide nanoparticles. *Nanotechnol. Sci. Appl.* **2016**, *9*, 49–67. [[CrossRef](#)]
13. Chen, C.Y.; Li, H.; Davis, M.M. Studies on mesoporous materials. *Microporous Mater.* **1993**, *2*, 17–26. [[CrossRef](#)]
14. Liu, Z.; Teng, Y.; Zhang, K.; Cao, Y.; Pan, W. CO₂ adsorption properties and thermal stability of different amine-impregnated MCM-41 materials. *J. Fuel Chem. Technol.* **2013**, *41*, 469–475. [[CrossRef](#)]
15. Luna, D.M.; Millanar, J.M.; Yodsanga, A.; Wantala, K. Gas phase Catalytic Oxidation of VOCS using Hydrothermally Synthesized Nest-like K-OMS 2 Catalyst. *Sains Malays.* **2017**, *46*, 275–283.
16. Zhao, S.; Yu, X.; Qian, Y.; Chen, W.; Shen, J. Multifunctional magnetic iron oxide nanoparticles: An advanced platform for cancer theranostics. *Theranostics* **2020**, *10*, 6278–6309. [[CrossRef](#)] [[PubMed](#)]

17. Gandhi, S.; Venkatesh, S.; Sharma, U.; Jagannathan, N.R.; Sethuraman, S.; Krishnan, U.M. Superparamagnetic nanosystems based on iron oxide nanoparticles & mesoporous silica: Synthesis & evaluation of their magnetic, relaxometric and biocompatibility properties. *J. Mater. Chem.* **2011**, *21*, 15698. [[CrossRef](#)]
18. Kalantari, S.; Yousefpour, M.; Taherian, Z. Synthesis of mesoporous silica/iron oxide nanocomposites and application of optimum sample as adsorbent in removal of heavy metals. *Rare Met.* **2016**, *36*, 942–950. [[CrossRef](#)]
19. Shon, K.J.; Soo, S.K.; Min, S.K.; Jii, M.K.; Byung, G.S. Synthesis of mesoporous iron oxide nanoparticles from mesoporous silica template via nano-replication. *Funct. Mater. Lett.* **2008**, *1*, 151–154. [[CrossRef](#)]
20. Hao, T.T.; Wai, R.S.; Leny, Y. Enhanced adsorption of acetylsalicylic acid over hydrothermally synthesized iron oxide-mesoporous silica MCM-41 composites. *J. Taiwan Inst. Chem. Eng.* **2016**, *65*, 591–598. [[CrossRef](#)]
21. Yousaf, Z.; Saleh, N. Advanced Concept of Green Synthesis of Metallic Nanoparticles by Reducing Phytochemicals. In *Nanobotany*; Springer: Cham, Switzerland, 2018; pp. 17–36. [[CrossRef](#)]
22. Nazar, A.P.; Licea, Y.E.; Colaço, M.V.; Senra, J.D.; Carvalho, N.M.F. Green iron oxides/amino-functionalized MCM-41 composites as adsorbent for anionic azo dye: Kinetic and isotherm studies. *J. Environ. Chem. Eng.* **2021**, *9*, 105062. [[CrossRef](#)]
23. Bouafia, A.; Laouini, S.E. Green synthesis of iron oxide nanoparticles by aqueous leaves extract of *Mentha pulegium* L.: Effect of ferric chloride concentration on the type of product. *Mater. Lett.* **2020**, *265*, 127364. [[CrossRef](#)]
24. Zúñiga, M.J.; Guerra, J.; Mueller, A.; Mayorga, R.A.; Carrera, P.S.E.; Barba, O.C.; Heredia, M.J.; Guamán, L.P. Iron Oxide Nanoparticles: Green Synthesis and Their Antimicrobial Activity. *Nanomaterials* **2023**, *13*, 2919. [[CrossRef](#)]
25. Karpagavinayagam, P.; Vedhi, C. Green synthesis of iron oxide nanoparticles using *Avicennia marina* flower extract. *Vacuum* **2019**, *160*, 286–292. [[CrossRef](#)]
26. Devi, H.S.; Boda, M.A.; Shah, M.A.; Parveen, S.; Wani, A.H. Green synthesis of iron oxide nanoparticles using *Platanus orientalis* leaf extract for antifungal activity. *Green Process. Synth.* **2019**, *8*, 38–45. [[CrossRef](#)]
27. Kumar, V.G.; Ananthu, P.A. Green Synthesis and Characterization of Iron Oxide Nanoparticles Using *Phyllanthus niruri* Extract. *Orient. J. Chem.* **2018**, *34*, 2583–2589. [[CrossRef](#)]
28. Das, S.; Chitta, R.P. *Green Synthesis of Iron Oxide Nanoparticles Using Plant Extracts and Its Biological Application*; Elsevier eBooks: Amsterdam, The Netherlands, 2021; Volume 2, pp. 139–170. [[CrossRef](#)]
29. Nagajyothi, P.C.; Pandurangan, M.; Kim, H.D.; Sreekanth, T.V.M.; Shim, J. Green Synthesis of Iron Oxide Nanoparticles and Their Catalytic and In Vitro Anticancer Activities. *J. Clust.* **2016**, *28*, 245–257. [[CrossRef](#)]
30. Bibi, I.; Nazar, N.; Ata, S.; Sultan, M.; Ali, A.; Abbas, A.; Jilani, K.; Kamal, S.; Sarim, F.M.; Khan, M.I.; et al. Green synthesis of iron oxide nanoparticles using pomegranate seeds extract and photocatalytic activity evaluation for the degradation of textile dye. *J. Mater. Res. Technol.* **2019**, *8*, 6115–6124. [[CrossRef](#)]
31. Niraimathe, V.A.; Subha, V.; Ravindran, R.S.E.; Renganathan, S. Green synthesis of iron oxide nanoparticles from *Mimosa pudica* root extract. *Int. J. Sustain. Dev.* **2016**, *15*, 227. [[CrossRef](#)]
32. Luna, P.M.; Alarcón, H.M.; Silva, S.M.; Rentería, V.M.; Rodríguez, V.M.; Herrera, P.E.; Reyes, C.M.; Montero, C.M. *Baccharis salicifolia* development in the presence of high concentrations of uranium in the arid environment of San Marcos, Chihuahua. *Rev. Mex. Fis.* **2011**, *57*, 40–43.
33. Haque, N.; Peralta, V.J.R.; Jones, G.L.; Gill, T.E.; Gardea, J.L. Screening the phytoremediation potential of desert broom (*Baccharis sarothroides* Gray) growing on mine tailings in Arizona, USA. *Environ. Pollut.* **2008**, *153*, 362–368. [[CrossRef](#)]
34. Li, T.; Yin, W.; Gao, S.; Sun, Y.; Xu, P.; Wu, S.; Kong, H.; Yang, G.; Wei, G. The Combination of Two-Dimensional Nanomaterials with Metal Oxide Nanoparticles for Gas Sensors: A Review. *Nanomaterials* **2022**, *12*, 982. [[CrossRef](#)]
35. Hasanzadeh, M.; Shadjou, N.; Omidinia, E. Mesoporous Silica (MCM-41)-Fe₂O₃ as a Novel Magnetic Nanosensor for Determination of Trace Amounts of Amino Acids. *Colloids Surf. B Biointerfaces* **2013**, *108*, 52–59. [[CrossRef](#)] [[PubMed](#)]
36. Cullity, B.D.; Stock, S.R. *Elements of X-ray Diffraction*, 3rd ed.; Prentice-Hall: New York, NY, USA, 2001.
37. Mohammed, A.; Ahmed, A.U.; Ibraheem, H.; Kadhom, M.; Yousif, E. Physisorption theory of surface area and porosity determination: A short review. *AIP Conf. Proc.* **2022**, *2450*, 02007. [[CrossRef](#)]
38. Bhushan, B. *Spectroscopic and Microscopic Techniques for Nanocharacterization*, 3rd ed.; Springer Handbook of Nanotechnology: Chattanooga, TN, USA, 2017.
39. Ramos, C.F.; Bressan, J.; Godoy, J.V.C.; Zuccolotto, T.; Da Silva, L.E.; Bonancio, C.L. *Baccharis* (Asteraceae): Chemical Constituents and Biological Activities. *Chem. Biodivers.* **2016**, *13*, 1–17. [[CrossRef](#)] [[PubMed](#)]
40. Manfron, J.; Raman, V.; Khan, I.A.; Paulo, V.F. *Essential Oils of Baccharis: Chemical Composition and Biological Activities*; Springer eBooks: New York, NY, USA, 2021; Volume 1, pp. 239–257. [[CrossRef](#)]
41. Flores, C.R.; Ponzi, M.I.; Ardanaz, C.E.; Tonn, C.E.; Donadel, O.J. Chemical composition of essential oil of *Baccharis salicifolia* (ruiz & pavon) pers. and antibacterial activity. *J. Chil. Chem. Soc.* **2009**, *54*, 475. [[CrossRef](#)]
42. Akintelu, S.A.; Oyebamiji, A.K.; Olugbeko, S.C.; Folorunso, A.S. Green synthesis of iron oxide nanoparticles for biomedical application and environmental remediation: A review. *Eclat. Quim.* **2021**, *46*, 17–37. [[CrossRef](#)]
43. Arnaud, D.; Panissod, P.; Pichon, B.P.; Pourroy, G.; Guillon, D.; Bertrand, D.; Begin, C.S. Size-dependent properties of magnetic iron oxidenanocrystals. *Nanoscale* **2011**, *3*, 225–232. [[CrossRef](#)]
44. Sharifi, D.H.; Halda, R.A.; Ersöz, B.; Tremel, W.; Jakob, G.; Asadi, K. Effect of precursor concentration on size evolution of iron oxide nanoparticles. *CrystEngComm* **2017**, *19*, 6694–6702. [[CrossRef](#)]

45. Guardia, P.; Pérez, N.; Labarta, A.; Batlle, X. Controlled Synthesis of Iron Oxide Nanoparticles over a Wide Size Range. *Langmuir* **2009**, *26*, 5843–5847. [[CrossRef](#)]
46. Li, Z.J.; Zhang, Y.J.; Zhang, H.W.; Fu, H.X. Long-lasting phosphorescence functionalization of mesoporous silica nanospheres by CaTiO₃:Pr³⁺ for drug delivery. *Microporous Mesoporous Mater.* **2013**, *176*, 48–54. [[CrossRef](#)]
47. Bernal, P.Y.; Alvarado, J.; Juárez, L.R.; Mendez, M.A.; Vasconcelos, A.E.; Mendes, W.A.; Iniesta, A.S.; Cab, V.J. Synthesis and characterization of MCM-41 powder and its deposition by spin-coating. *Optik* **2019**, *185*, 429–440. [[CrossRef](#)]
48. Rouquerol, J.; Rouquerol, F.; Llewellyn, P.; Maurin, G.; Kenneth, S.W. *Adsorption by Powders and Porous Solids*; Academic Press: Cambridge, MA, USA, 2013.
49. Ravikovitch, P.I.; Neimark, A.V. Characterization of nanoporous materials from adsorption and desorption isotherms. *Colloids Surf. A Physicochem. Eng. Asp.* **2001**, *187–188*, 11–21. [[CrossRef](#)]
50. Dollimore, D.; Heal, G.R. An improved method for the calculation of pore size distribution from adsorption data. *J. Appl. Chem.* **2007**, *14*, 109–114. [[CrossRef](#)]
51. Thommes, M.; Kaneko, K.; Neimark, A.V.; Olivier, J.P.; Rodriguez, R.F.; Rouquerol, J.; Sing, K.S.W. Physisorption of gases, with special reference to the evaluation of surface area and pore size distribution. *Pure Appl. Chem.* **2015**, *87*, 1051–1069. [[CrossRef](#)]
52. Turcheniuk, K.; Tarasevych, A.V.; Kukhar, V.P.; Boukherroub, R.; Szunerits, S. Recent advances in surface chemistry strategies for the fabrication of functional iron oxide based magnetic nanoparticles. *Nanoscale* **2013**, *5*, 10729. [[CrossRef](#)] [[PubMed](#)]
53. Shi, L.; Wang, K.; Yang, C.; Qian, H.; Liu, D.; Pan, R. Synthesis, characterization of Nafion-functionalized MCM-41 and its catalytic application in preparation of CL-20 via HNO₃ electrolyte involved nitration of TAIW. *J. Saudi Chem. Soc.* **2018**, *22*, 588–593. [[CrossRef](#)]
54. Nalbandian, L.; Patrikiadou, E.; Zaspalis, V.; Patrikidou, A.; Hatzidaki, E.; Papandreou, C. Magnetic Nanoparticles in Medical Diagnostic Applications: Synthesis, Characterization and Proteins Conjugation. *Curr. Nanosci.* **2016**, *12*, 455–468. [[CrossRef](#)]
55. Sobhanardakani, S.; Jafari, A.; Zandipak, R.; Meidanchi, A. Removal of heavy metal (Hg(II) and Cr(VI)) ions from aqueous solutions using Fe₂O₃@SiO₂ thin films as a novel adsorbent. *Process Saf. Environ.* **2018**, *120*, 348–357. [[CrossRef](#)]
56. Bali, O.A.; Kianvash, A.; Hajalilou, A.; Abouzari, L.E.; Zarebkohan, A. Cytotoxicity characteristics of green assisted-synthesized superparamagnetic maghemite (γ-Fe₂O₃) nanoparticles. *J. Mater. Sci. Mater. Electron.* **2018**, *29*, 12135–12143. [[CrossRef](#)]
57. Migliorato, P.; Correia, L.P.M. Detection of Molecular Interactions Using a Metal-Insulator-Semiconductor Diode Structure. Patent WO2005036156A1, 21 April 2005.
58. Da, R.; Camilo, F.F.; Bizeto, M.A. Evaluation of the influence of sulfur-based functional groups on the embedding of silver nanoparticles into the pores of MCM-41. *J. Solid State Chem.* **2016**, *235*, 125–131. [[CrossRef](#)]
59. Jaroniec, M. A new method for the accurate pore size analysis of MCM-41 and other silica based mesoporous materials. *Stud. Surf.* **2000**, *128*, 71–80. [[CrossRef](#)]
60. Luciano, B.G.; Panecatl, B.Y.; Soto, C.S.; Méndez, R.M.A.; López, S.P.; Alcántara, I.S.; Chávez, P.M.; Romero, L.A.; Mejía, S.J.; Alvarado, J.; et al. Controlling Size Distribution of Silver Nanoparticles using Natural Reducing Agents in MCM-41@Ag. *ChemistrySelect* **2022**, *7*, e202202566. [[CrossRef](#)]
61. Liu, Y.; He, Q.; Li, Y.; Li, Y.; He, C. Synthesis of copper-based nanoparticles confined in a pyridine N-containing COF and their catalytic applications. *Microporous Mesoporous Mater.* **2024**, *364*, 112868. [[CrossRef](#)]
62. Schroder, D. *Semiconductor Material and Device Characterization*, 3rd ed.; John Wiley Inc.: Hoboken, NJ, USA, 2018; pp. 278–281.
63. Dominguez, M.A.; Luna, J.A.; Ceron, S. Low-temperature ultrasonic spray deposited aluminum doped zinc oxide film and its application in flexible Metal-Insulator-Semiconductor diodes. *Thin Solid Films* **2018**, *645*, 278–281. [[CrossRef](#)]

Disclaimer/Publisher’s Note: The statements, opinions and data contained in all publications are solely those of the individual author(s) and contributor(s) and not of MDPI and/or the editor(s). MDPI and/or the editor(s) disclaim responsibility for any injury to people or property resulting from any ideas, methods, instructions or products referred to in the content.